THE JOURNAL OF PHYSICAL CHEMISTRY C
A JOURNAL OF THE AMERICAN CHEMICAL SOCIETY

pubs.acs.org/JPCC

Article

H_2O Promoted the Photocatalytic Toluene Oxidation at Ambient Humidity on Zn-Doped K-OMS-2: Mechanism Study

Xiaoshan Zeng, Zehui Huang, Xiaoqian Wei, Pingping Yu, Weixin Zou,* Qing Tong,* Bin Gao, and Lin Dong

Cite This: *J. Phys. Chem. C* 2024, 128, 16522−16531

Read Online

ACCESS | Metrics & More | Article Recommendations | Supporting Information

ABSTRACT: The poor stability of the MnO_2 catalyst limits its application in photocatalytic toluene oxidation, especially at ambient humidity. Herein, the doped Zn^{2+} attached to the tunnel of K-OMS-2 by replacing K^+ (Zn-KM photocatalyst) with an appropriate hydrophilicity surprisingly exhibits better photocatalytic performance and stability for the toluene oxidation at ambient humidity than that of KM. Especially, at a higher RH of 42%, Zn-KM shows approximately double the times of toluene removal (80%) than KM, with an excellent stability for at least 8 h. Comprehensive characterizations and calculations suggest that on the Zn-KM photocatalyst, the H_2O molecule significantly reduces the adsorption energy of toluene (from −3.38 to −3.72 eV) via the hydrogen bond−mediated intermediate; simultaneously, its enhanced average Mn−O bond (from 2.27 to 2.20 Å) forms the intensive built-in electric field and promotes faster electron transfer, leading to more oxygen radical generation, richer key ring-opening intermediate of alkoxide species, and an increased stability. However, the strongly hydrophilic KM photocatalyst has easier H_2O adsorption (−1.19 eV), inhibiting toluene adsorption and oxidation. This work provides the economic viability of MnO_2-based photocatalysts for toluene removal.

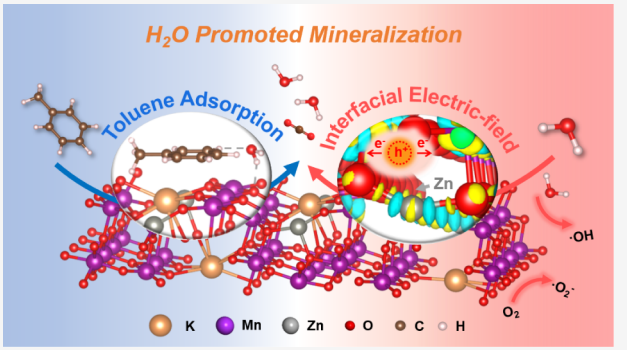

1. INTRODUCTION

With the advancement of technology and industry, the demand for improved living conditions has increased over the past few decades. Indoor volatile organic compounds (VOCs), which originate from various sources such as furniture, paints, solvents, varnishes, and preservatives,[1] have garnered significant attention. Long-term exposure to high levels of VOCs may lead to various health problems such as nausea and vomiting, skin allergy, and even cancer.[2] Toluene, as a common and carcinogenic indoor air pollutant, has posed a great threat to human health.[3] Many studies have been conducted on the removal of toluene in order to reduce VOC concentrations in indoor environment. Air pollution removal methods such as adsorption,[4] thermal catalytic oxidation,[5] and photocatalytic oxidation[6] have been applied. Due to its mild reaction conditions, excellent performance, and reasonable economy, heterogeneous photocatalysis is regarded as one of the most promising strategies for toluene removal.[7,8]

Generally, metal oxides are the most effective catalysts for toluene oxidation due to their superior redox performance, low cost, and changeable valence states. Among many non-noble metal oxides,[9−12] manganese dioxide (MnO_2) is regarded as a promising material due to its rich oxygen vacancy, various Mn species, excellent redox ability, and oxygen storage.[13] Therefore, some research on the utilization of MnO_2 for air pollutant removal has been reported, such as formaldehyde,[14] ethanol,[15] benzene,[16] and toluene.[17]. Nanostructured cryptomelane-type manganese oxide octahedral molecular sieves (K-OMS-2) belonging to α-MnO_2 attract a lot of attention in the catalytic area due to their excellent redox properties.[18] Because of the special tunnel structure, they also serve as a reservoir for ions. The strain effect, which could tune the electronic structure by changing the distance between the atoms on the surface and in turn change the catalytic activity, widely exists in K-OMS-2.[19] However, it is found that although pure K-OMS-2 has superior redox, its reaction stability is poor. Therefore, many strategies are used to modify it.

It is reported that a wide variety of ions (e.g., Fe^{3+}, Co^{2+}, Ni^{2+}, Cu^{2+}, and Zn^{2+}) could be trapped into K-OMS-2 to render novel physical and chemical properties.[19] Among them, the Zn/MnO_2 batteries have been extensively investigated, and elemental zinc is commonly used as the negative electrode in aqueous electrolyte batteries. During the charging and

Received: August 6, 2024
Revised: September 9, 2024
Accepted: September 11, 2024
Published: September 20, 2024

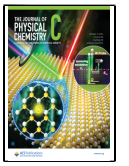

https://doi.org/10.1021/acs.jpcc.4c05307
J. Phys. Chem. C 2024, 128, 16522−16531

discharging periods, Zn^{2+} can get inserted into the tunnel of MnO_2. Alfaruqit et al.[20] reported a relatively reversible Zn^{2+} insertion for γ-MnO_2. In their further research,[21] it was found that α-MnO_2 electrode retained considerable structural stability toward Zn^{2+} insertion and exhibited nearly 100% Columbic efficiencies over prolonged cycling. On the basis of the abovementioned studies, it is proposed that the Zn^{2+} insertion into the tunnel of OMS-2, with a high stable structure and electron transfer ability, acts as a potential photocatalyst, and the effects of Zn^{2+} insertion on toluene removal are worth investigating.

In indoor toluene removal, water vapor inevitably exists with changeable relative humidity values. Generally, water vapor has different effects on toluene removal, according to the relative humidity (RH) values, photocatalyst structures, etc. For the MnO_2 catalyst, its toluene oxidation efficiency is often suppressed at ambient humidity. Therefore, many strategies are used to modify MnO_2 to improve the performance of toluene oxidation under water vapor conditions. For example, Zhang et al.[22] prepared Ce-MnO_2 using ion exchange, which exhibited better catalytic activity with H_2O vapor at low temperatures. In addition, the $MnCeO_x$ catalysts via the Ce-BTC pyrolysis showed superior catalytic stability under high humidity due to water vapor on $MnCeO_x$, promoting oxygen activation.[23] However, a simple method of ion doping MnO_2 to improve the performance of toluene removal at ambient humidity has been less achieved, and the mechanism of H_2O-promoted toluene oxidation on the ion doping MnO_2 is unclear.

Herein, due to the advantage of Zn^{2+} insertion into the tunnel of OMS-2 with a high stable structure and electron transfer ability, the Zn^{2+}-doped K-OMS-2 by replacing K^+ (Zn-KM photocatalyst) was synthesized via a simple hydrothermal method, which exhibited improved photocatalytic performance of toluene oxidation in RH from 10% to 50%. Surprisingly, compared with the pure KM, the introduction of H_2O under the reaction conditions increased the toluene removal on the Zn-KM photocatalyst instead of the decreased performance. With the help of experimental characterizations and DFT calculations, the location of Zn^{2+} in K-OMS-2 was identified, and the influences of Zn^{2+} on the electronic charges of Mn species, H_2O and toluene adsorption, oxygen mobility, generated oxygen-contained radicals, and reaction intermediates were, respectively, explored. Furthermore, the reaction mechanism of the H_2O-promoted performance for toluene oxidation was revealed. This work provides guidance for designing efficient Mn-based photocatalysts for toluene removal at ambient humidity.

2. METHODS

2.1. Synthesis of Photocatalysts. *K-OMS-2 nanorods*: The K^+-modified cryptomelane-type octahedral molecular sieve (K-OMS-2) nanorods were synthesized via a hydrothermal reaction. At first, $KMnO_4$ (1.66 g) and $MnSO_4{\cdot}H_2O$ (2.48 g) were mixed with deionized water (75 mL). Then, the abovementioned mixture was sealed in a 150-mL Teflon-lined autoclave, followed by hydrothermal treatment at 160 °C for 4 h. Subsequently, the precipitates were washed with deionized water and ethanol several times, respectively, and were dried at 110 °C for 12 h. Finally, the powder was calcinated at 300 °C in air for 6 h.

Zn-KM nanorods: The synthesis procedures of Zn-KM nanorods were similar to the abovementioned process of K-OMS-2, with the exception of using $Zn(NO_3)_2{\cdot}6H_2O$, which was dissolved in a mixture of H_2O and HNO_3 (V_{H_2O}: V_{HNO_3} = 25: 1) in the required amounts. The molar doping ratio of Zn^{2+} was chosen as 6%, 10%, and 20%, respectively.

2.2. Characterizations. Details of the characterizations of X-ray diffraction (XRD), scanning electron microscope (SEM), X-ray photoelectron spectroscopy (XPS), diffuse reflectance spectroscopy (DRS), inductively coupled plasma optical emission spectrometer (ICP-OES), photoluminescence (PL) spectra, O_2-temperature-programmed desorption (O_2-TPD), mass spectrometer (MS), H_2-programmed temperature rise reduction (H_2-TPR), electron spin resonance (ESR), and *in situ* diffuse reflectance infrared Fourier transform spectroscopy (*in situ* DRIFTS) are available in the Supporting Information. The photoelectrochemical measurements were conducted using a standard three-electrode cell on a CHI660E electrochemical workstation. The test conditions were according to those reported in previous studies.[7,24]

2.3. Photocatalytic Toluene Oxidation. The photocatalytic oxidation of toluene was conducted in a 1.5-L cylindrical reactor using a 300 W xenon lamp as the light source. Catalyst powder (50 mg) was uniformly distributed on a 304 mm stainless steel mesh. The reaction gas toluene (50 $mL{\cdot}min^{-1}$) was maintained at a concentration of 30 ppm by a balance of high-purity air (21% O_2, balanced with N_2), which was continuously vented into the reactor at a specific relative humidity value (RH = 13%, 22%, and 42%), which was controlled by the ratio of water vapor and air during the reaction process and flowed through the stainless steel mesh lined with the catalyst and then into the gas chromatography column for detection. Photoreaction was initiated by adsorption for 40 min in dark, followed by photocatalytic toluene oxidation under 300 W xenon lamp irradiation, and the reaction performance was obtained using chromatography. The toluene conversion was calculated as follows:

$$C_7H_8 \text{ conversion } (\%) = \frac{[C_7H_8]_{in}\text{-}[C_7H_8]_{out}}{[C_7H_8]_{in}} \times 100\%$$

where $[C_7H_8]_{in}$ and $[C_7H_8]_{out}$ represent the concentrations (ppm) of inlet and outlet gas phase toluene, respectively.

2.4. Details of Density Functional Theory (DFT) Calculations. We used the Vienna Ab Initio Package (VASP)[25,26] to conduct spin-polarized DFT calculations in the generalized gradient approximation (GGA) using the PBE[27] formulation. For the ionic cores, we opted for projected augmented wave (PAW) potentials[28,29] and accounted for valence electrons using a plane wave basis set with a kinetic energy cutoff of 400 eV. Partial occupancies of the Kohn–Sham orbitals were permitted using the Gaussian smearing method and a width of 0.05 eV. The electronic energy was deemed self-consistent if the energy change was less than 10^{-5} eV. A geometry optimization was considered to be converged if the force change was less than 0.02 eV/Å. To describe the dispersion interactions, Grimme's DFT-D3 methodology was utilized.[30]

The lattice constants of the tetragonal α-MnO_2 unit cell doped with K atoms were optimized to a = 9.993 and c = 5.898 Å to form model 1. Model 2, a 1 × 1 × 2 supercell of model 1, has half of its K atoms substituted for Zn atoms. Model 3 is a 1 × 1 × 2 supercell of model 1 with two Mn atoms replaced by Al atoms. All atoms were permitted to relax, and a 2 × 2 × 2 k-

https://doi.org/10.1021/acs.jpcc.4c05307
J. Phys. Chem. C 2024, 128, 16522−16531

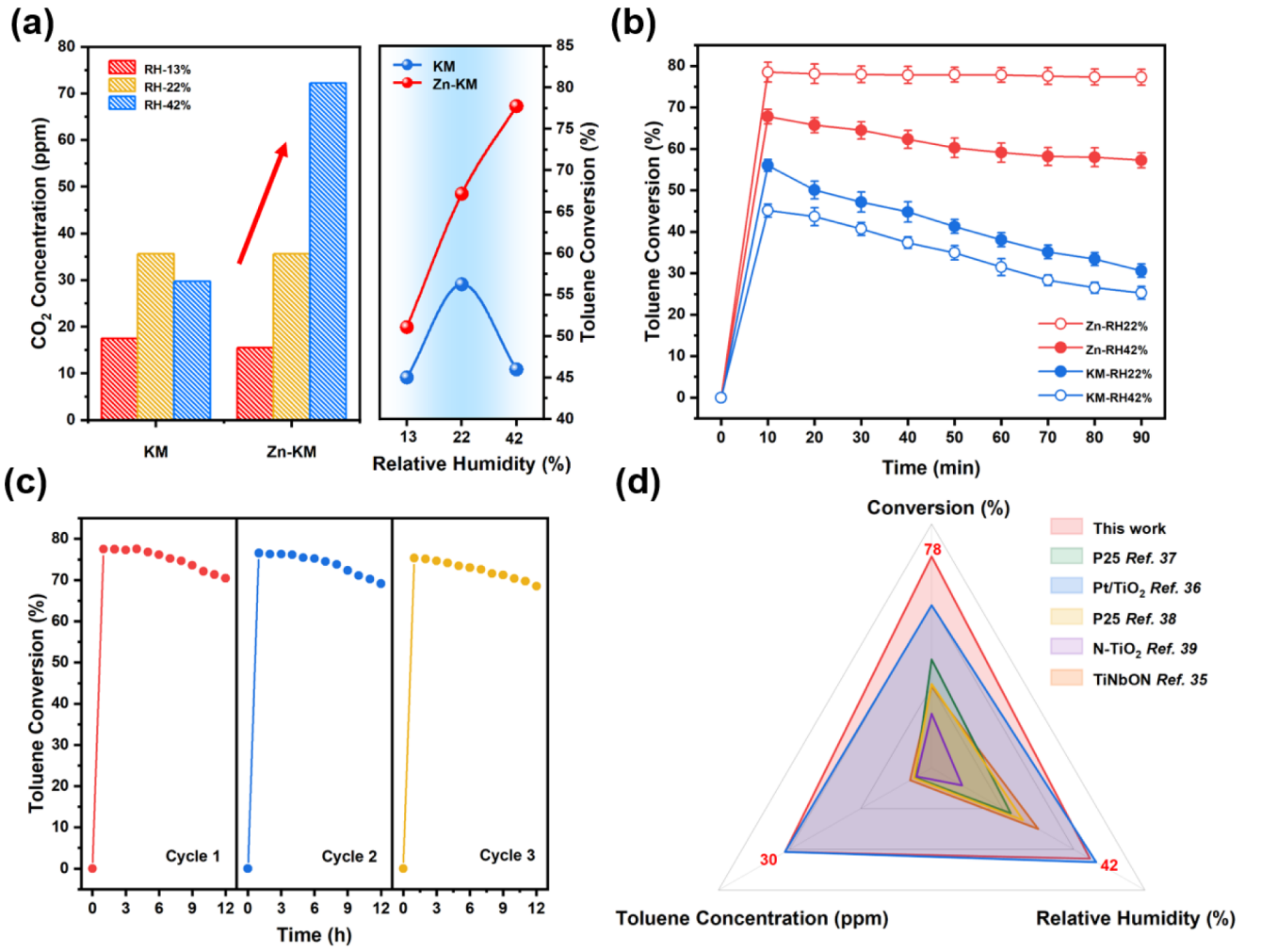

Figure 1. (a) Photocatalytic activities of toluene oxidation and (b) toluene conversion over different RH condtions of KM and Zn-KM under xenon lamp illumination. (c) Cycle test over Zn-KM with RH = 42% and (d) the performance comparison of photocatalytic toluene oxidation with that found in the literature.[35−39].

point grid was utilized for k-point sampling during structural optimization in the Brillouin zone.

The atomic charges were obtained through the Bader's analysis[31] using the numerical implementation developed by Henkelman et al.[32] VESTA visualization code was used to generate the charge density differences, calculated as $\Delta\rho(r) = \rho total(r) - \rho A(r) - \rho B(r)$. Here, $\rho_{total}(r)$ represents the electron density of the Pt-doped graphene support, $\rho_A(r)$ represents the electron density of doped atoms, and $\rho_B(r)$ represents the electron density of the model featuring the doped atoms.

3. RESULTS AND DISCUSSION

3.1. Morphology and Texture Properties. The morphologies of K-OMS-2 (KM) and Zn-KM were determined by SEM characterization (Figure S1). The images showed that both KM and Zn-KM exhibited nanowire shapes with a length of ca. 1 μm. Different from the KM nanowires with a smooth surface and longer length, Zn-KM maintained with shorter nanowires, which can attribute to the foreign ions affecting the growth of nanowires.[19] In addition, the specific surface areas of KM and Zn-KM were determined, which were 51.5 and 64.6 $m^2 \cdot g^{-1}$, respectively. There was a slight increase in the surface area compared with that of KM, resulting from the disordering effect caused by Zn^{2+} ion storage. Moreover, the phase structures of KM and Zn-KM were investigated by the XRD characterization. In Figure S2, this pattern revealed that all the as-synthesized samples were indexed to pure α-MnO_2 (JCPDS, PDF#44−0141), which is a type of well-defined 2 × 2 tunnel size of ~4.6 Å. The peaks at 12.784°, 18.107°, 28.841°, 37.522°, 41.968°, 49.864°, 56.372°, and 60.274° corresponded to (110), (200), (310), (211), (301), (411), (600), and (521), respectively. It was found that the ion storage of Zn^{2+} did not cause a significant change in the crystal phase of samples.

Furthermore, the location of Zn^{2+} in KM was analyzed through the ion exchange experiments several times to explore. Generally, the weaker coordination bonds and higher water contact rate of the ions in the tunnel of KM were easily washed out by water, while the ions in the skeletons of KM by replacing Mn^{4+} were more difficult to wash out due to their stronger coordination bonds and inner position.[33,34] Therefore, the method of ion exchange was used in Zn-KM, which was constant stirring for 18 h with the deionized water three times. Subsequently, the concentrations of Zn^{2+} ions in the exchanged water were determined by the ICP analysis. It was found that under washing conditions, the Zn^{2+} ions were washed out in water several times. The calculated losing Zn^{2+}

https://doi.org/10.1021/acs.jpcc.4c05307
J. Phys. Chem. C 2024, 128, 16522−16531

ions in Zn-KM were 9.01%, which was almost similar to K^+ (10.91%) in KM. Based on the previous conclusion,[33,34] it was demonstrated that the doped Zn^{2+} ions were attached to the tunnel of K-OMS-2 by replacing K^+ ions. Therefore, the Zn-doped K-OMS-2 (Zn-KM) photocatalyst was successfully synthesized via a simple hydrothermal method, which was used for the photocatalytic oxidation of toluene.

3.2. Photocatalytic Performance of Toluene Oxidation. The photocatalytic efficiencies of toluene removal on KM and Zn-KM samples with different doping ratios were evaluated under simulated solar light with a full spectrum. As shown in Figure S3a, the catalyst with the 10% doping ratio exhibited the best oxidation activity when the relative humidity was 42%, and $Zn_{0.1}$-KM exhibited considerable stability, as displayed in Figure S3b. Therefore, we chose $Zn_{0.1}$-KM and KM to further investigate the doped effects on toluene removal at ambient humidity. Moreover, the photocatalytic conversion of toluene oxidation under different relative humidity (RH) conditions were determined (Figure 1a,b). Notably, water vapor did not cause a decrease in the catalytic performances on Zn-KM, instead enhanced toluene conversion with increased RH, whereas KM had reduced activities at ambient humidity. Moreover, as the RH became higher, Zn-KM was able to realize more CO_2 product and the mineralization rate was improved. When the RH was from 22% to 42%, the toluene conversion of Zn-KM increased from 68% to 80%, but the KM displayed undesirable stability, decreasing from 56% to only 30%. When irradiated by visible light only, the activity of the catalyst is still maintained at high stability, with a strong ability to adapt to the environment (Figure S4). Furthermore, the catalytic stability of Zn-KM in toluene oxidation can be observed for at least 36 h, with three cycles (Figure 1c). Compared to previous literature,[35−39] Zn-KM showed considerable catalytic activity for toluene removal at ambient humidity (Figure 1d). The enhanced mechanism of photocatalytic toluene oxidation under the condition with H_2O on Zn-KM was explored in detail, compared with KM.

3.3. Formed Lewis Acid for Toluene Adsorption. For the gas−solid multiphase photocatalytic reaction, effective toluene adsorption on the catalyst plays an important role in the subsequent surface reactions. Therefore, *in situ* DRIFTS and DFT calculations of toluene adsorption were carried out. *In situ* DRIFTS of toluene adsorption on KM and Zn-KM are shown in Figure 2a. Obviously, the typical bands of toluene adsorption displayed from 1000 to 2000 cm^{-1}.[40,41] And the bands at 1506, 1540, and 1646 cm^{-1} represented the typical aromatic ring vibrations.[41] It could be observed that there were no obvious differences in the bands that appeared in the two samples, except for the band intensity. The adsorption intensity of Zn-KM was higher than that of KM, which indicated that Zn^{2+} doping could provide more adsorption sites on the catalyst surface for toluene molecules. Furthermore, the adsorption energies of toluene were calculated by the DFT method (Figure 2b), which were −0.22 eV and −3.38 eV for KM and Zn-KM, respectively. The lower energy suggested that Zn-KM was more facilitated to absorb toluene than KM, which might be due to a strong interaction between the π electrons (toluene) with Lewis acidic sites (Zn-KM surface).[42]

Generally, Mn^{4+} species in KM, as a kind of typical Lewis acid site, play an important role in toluene adsorption.[43,44] Therefore, the XPS spectra were used to analyze the surface Mn^{4+} species. In Figure 3a, the broad peak of the Mn $2p_{3/2}$ orbit was split into two peaks: 642.0 eV for Mn^{3+} and 644.5 eV

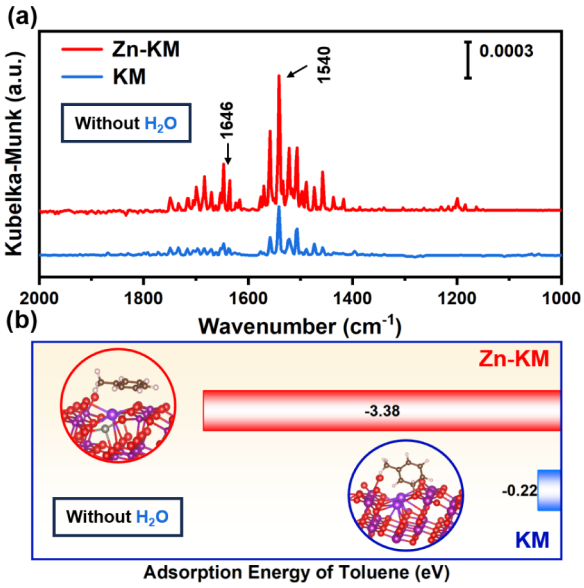

Figure 2. (a) *In situ* DRIFTS analysis of toluene adsorption without H_2O and (b) DFT calculations of adsorption energies of toluene without H_2O on Zn-KM and KM.

for Mn^{4+}.[45,46] It was found that the binding energies of Mn species on KM and Zn-KM had no obvious change, but the ratios of Mn^{4+}/Mn^{3+} were different, i.e., 22% in Zn-KM and 14% in KM. The abovementioned results suggested that after Zn^{2+} doping, there was much more Mn^{4+} on the catalyst surface, acting as Lewis acidic sites for more toluene adsorption. The H_2-TPR was further conducted to confirm more Mn^{4+} in Zn-KM. In Figure S5, a broad H_2 consumption peak of catalysts could split into two subpeaks, representing different valence states of Mn species. According to literature and our previous work,[47−49] the peak at lower temperature (approximately 320 °C) belonged to the signal of MnO_2 to Mn_2O_3, while the other at approximately 353 °C corresponded to Mn_2O_3 to Mn_3O_4. The valence states of Mn species presented mostly Mn^{4+} or Mn^{3+}, and the reduction area in H_2-TPR could roughly represent the ratios of Mn^{3+} to Mn^{4+},[50,51] which was 68.3% in Zn-KM, as 1.58 times as KM (43.1%). It can also demonstrate that there were more Mn^{4+} in Zn-KM, which was consistent with the XPS results.

Specifically, DFT calculations were conducted to clearly clarify the electron densities of Mn atoms to confirm more Mn^{4+} species in Zn-KM. Differential charge densities were calculated to theoretically analyze the charge accumulation and depletion. As shown in Figure 3b, after Zn^{2+} exchange of the K^+ in the KM tunnel, the electron cloud surrounding the manganese atom turned to reduced. This phenomenon indicated that there were fewer electrons surrounding the manganese atoms, resulting in more Mn^{4+} in Zn-KM, which could act as Lewis acid sites to absorb toluene,[52−54] compared to KM. In addition, the Bader charges of atoms can accurately demonstrate regarding the gain or loss of electrons and precisely figure out the electron arrangement at an atomic level.[55,56] To investigate the exact loss-gain number of electrons, we calculated the Bader charges of Mn, O, and Zn atoms. The results are shown in Figure 3c, and the average Bader charge for oxygen atom reduced from −0.904 to −0.934. Meanwhile, the manganese average Bader charge had a rise from 1.695 to 1.735. In Zn-KM, after the Zn^{2+} exchanged the

https://doi.org/10.1021/acs.jpcc.4c05307
J. Phys. Chem. C 2024, 128, 16522−16531

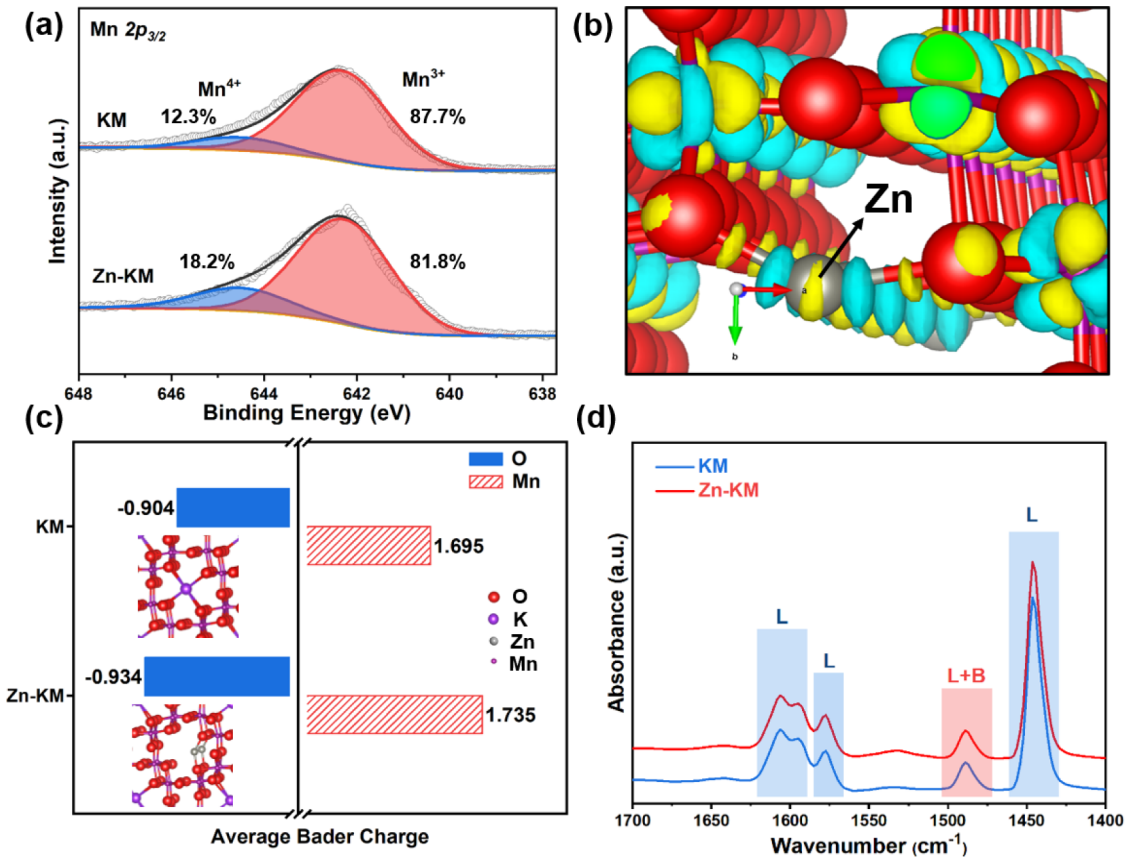

Figure 3. (a) XPS spectra of Mn $2p_{3/2}$ for KM and Zn-KM. (b) Differential charge densities of Zn-KM (yellow: charge accumulation; green: charge depletion). (c) The average Bader charge. (d) Py-IR spectra of KM and Zn-KM.

K^+ in the tunnel, electrons around the O atoms increased, while the electrons around the Mn atoms decreased, further leading to richer Mn^{4+} in Zn-KM. Furthermore, the pyridine infrared (Py-IR) spectra were used to investigate the Lewis acid sites. In Figure 3d, three peaks at 1445, 1575, and 1607 cm^{-1} corresponded to the Lewis acid sites.[57,58] As summarized in Table S1, the Lewis acid site amount of Zn-KM was 59.24 $\mu mol \cdot g^{-1}$, which was richer than that of KM, Therefore, the doped Zn^{2+} attached to the tunnel of K-OMS-2 by replacing K^+ generated richer Mn^{4+} species in Zn-KM, which acted as the Lewis acid sites to promote toluene adsorption.

3.4. H_2O-Promoted Effect. The adsorption and oxidation of toluene on the photocatalyst is related to the humidity, which is affected by the surface hydrophilicity, and thus, the H_2O adsorption ability on photocatalysts was determined by the water contact angles and DFT calculations. Figure S6 displays the water contact angles of KM and Zn-KM. It could be observed that compared with KM, the Zn-KM photocatalyst displayed a higher water contact angle, increasing from 19.8° to 36.3°, which meant that H_2O was harder to be adsorbed on Zn-KM than that on KM. In addition, we calculated the adsorption energies of H_2O on Zn-KM and KM samples. In Figure 4a, after doping Zn^{2+} into the tunnel of KM, the H_2O adsorption energies on Zn-KM and KM were −0.54 and −1.19 eV, respectively, combined with the toluene adsorption energies on Zn-KM (−3.38 eV) and KM (−0.22 eV). The result showed that under the condition of H_2O or toluene, KM was preferential for the adsorption of H_2O, not toluene, which inhibited the toluene adsorption and oxidation. While, on Zn-KM, due to its appropriate hydrophilicity, it is much easier to adsorb toluene than H_2O.

Furthermore, the toluene adsorption abilities in the presence of H_2O on KM and Zn-KM photocatalysts were also determined by *in situ* DRIFTS and DFT calculations in comparison. In the *in situ* DRIFTS of toluene adsorption under humidity condition (Figure 4b), the band at approximately 1130 cm^{-1} might be aroused by stronger dimer toluene molecule interactions with H_2O, which was estimated as the interplanar distance of the forming dimers via the substantial $\pi-\pi$ interactions between the aromatic rings of toluene,[59,60] and a theoretical work[61] had demonstrated that the π system of heterocycles can interact with H_2O to serve as proton acceptors. Herein, the signal at 1130 cm^{-1} of Zn-KM was stronger than that of KM, which meant that the introduction of H_2O did not disturb the adsorption of toluene, but promoted it. In addition, the peak at 1436 cm^{-1} attributed to toluene adsorption was blue shifted slightly at humidity, compared to that at dry condition, which might be caused by the hydrogen bond interaction between H_2O and toluene. Moreover, we conducted DFT calculations to confirm the H_2O effect on the toluene adsorption of Zn-KM (Figure 4c). It was found that in the presence of H_2O, there was a decreased energy (from −3.38 eV to −3.72 eV) of toluene adsorption on Zn-KM, while the value on KM rose from −0.22 to 2.80 eV. Therefore, on the Zn-KM photocatalyst, the H_2O molecule significantly reduced the adsorption energy of toluene on Zn-KM via the hydrogen bond interaction, whereas the strongly hydrophilic KM photocatalyst had easier H_2O adsorption (−1.19 eV), inhibiting toluene adsorption and oxidation. As analyzed

https://doi.org/10.1021/acs.jpcc.4c05307
J. Phys. Chem. C 2024, 128, 16522−16531

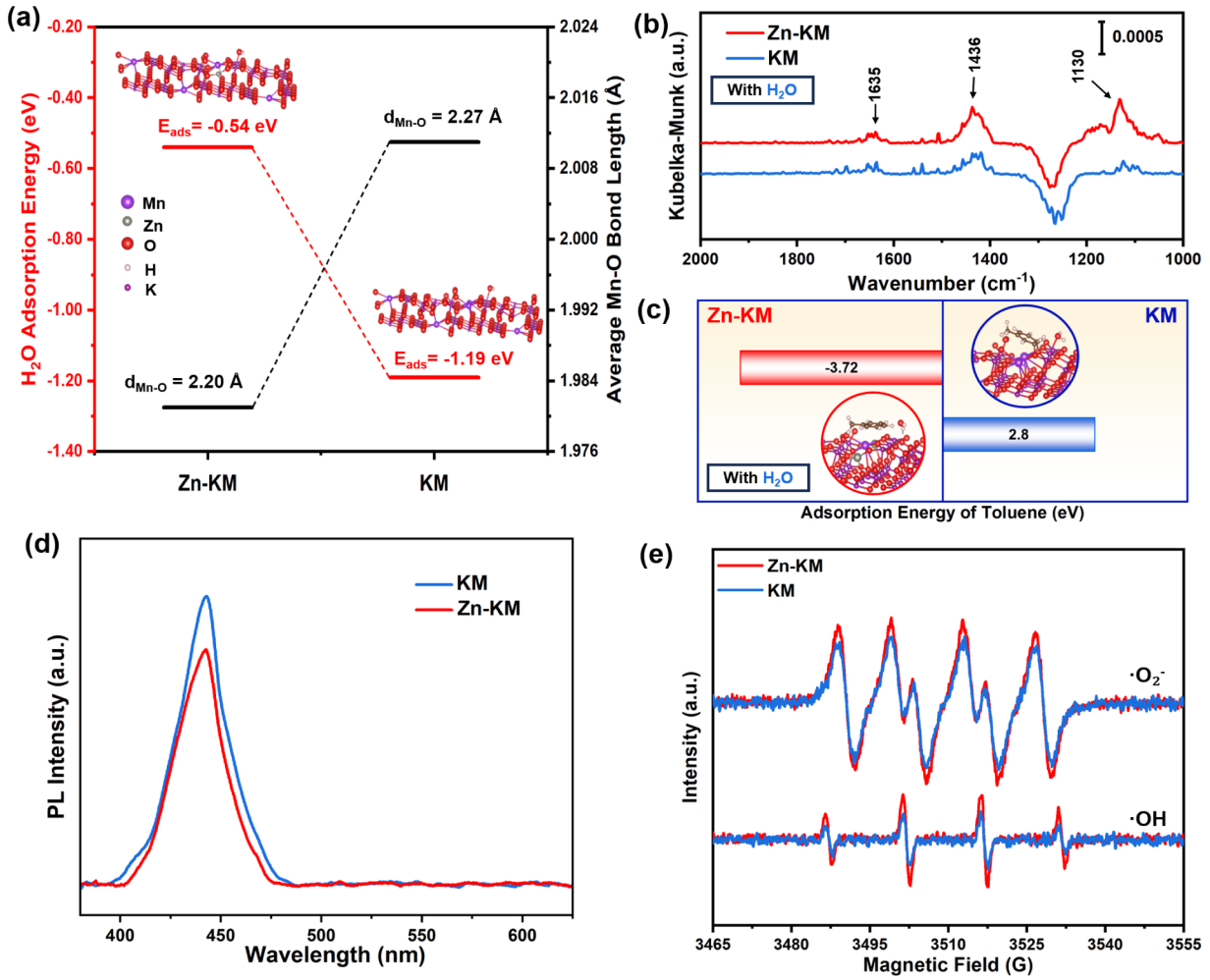

Figure 4. (a) Adsorption energy and the average Mn−O bond length with H_2O. (b) *In situ* DRIFTS analysis of toluene adsorption with H_2O. (c) DFT calculations of the adsorption energy of toluene with H_2O. (d) PL and (e) DMPO ESR spectra under light irradiation for 10 min for $\cdot O_2^-$ and ·OH on KM and Zn-KM.

above, the appropriate hydrophilicity of Zn-KM led to the weak competitive adsorption of H_2O and toluene; interestingly, instead, its adsorbed H_2O can improve the toluene adsorption through the hydrogen bond. Whereas on KM, H_2O would preemptively occupy the surface and thus further prevent the adsorption of toluene.

The presence of H_2O also affected the Mn−O bond of the photocatalyst. In Figure 4a, the average Mn−O bond length (2.20 Å) on Zn-KM surface was shorter with H_2O adsorption, compared with that on KM (2.27 Å), suggesting that the Mn−O bond on Zn-KM became stronger with the adsorbed H_2O. In general, the enhancement of the Mn−O bond promotes the electron transfer between the surface Lewis acid sites (manganese cations) and the adsorption reaction intermediates,[19] which can donate electrons to oxygen effectively, thereby forming the driving force for the surface O_2^-/−OH species and accelerating the conversion of the Mn^{3+}/Mn^{4+} couple.[62] As shown in Figure 4d, because of the H_2O-promoted intensive built-in electric field, more electron−hole pairs in Zn-KM can remain for a longer life cycle. And the PL and EIS Nyquist spectra (Figures 4d and S7) suggested that more electron−hole pairs exist on Zn-KM, which can participate in the reactions.[63] Therefore, besides H_2O-promoted toluene adsorption, H_2O can also enhance the built-in electric field on Zn-KM, leading to faster charge transfer for reactive oxygen species (ROS) generation in photocatalytic toluene oxidation.

The ROS was further analyzed by the ESR characterization. The ·OH radical is the main radical to participate in the toluene ring-opening process.[64−66] As shown in Figure 4e, the ·OH signal of Zn-KM is stronger than that of KM, owing to better electron−hole separation and more sufficient light utilization (Figures 4d and S7−S8). Furthermore, the higher intensity of $\cdot O_2^-$ on Zn-KM illustrated richer photoexcited electrons and better activation of oxygen. Therefore, the amount of $\cdot O_2^-$ and ·OH produced by Zn-KM was more than that of KM, resulting from faster charge transfer in the H_2O-enhanced built-in electric field, leading to better toluene oxidation.

3.5. Reaction Mechanism. *In situ* DRIFTS experiments under light illumination were conducted to analyze the photocatalytic mechanism of toluene oxidation with H_2O. As shown in Figure 5a,c, the typical characteristic peaks of toluene aromatic ring vibrations appeared at 1506 and 1540 cm^{-1}, indicating toluene adsorption.[40] With the increase in illumination time, various new species appeared, including the C−O vibration of the benzyloxy group with different adsorption models (1056, 1124, 1164, and 1184 cm^{-1}), COO^-

https://doi.org/10.1021/acs.jpcc.4c05307
J. Phys. Chem. C 2024, 128, 16522−16531

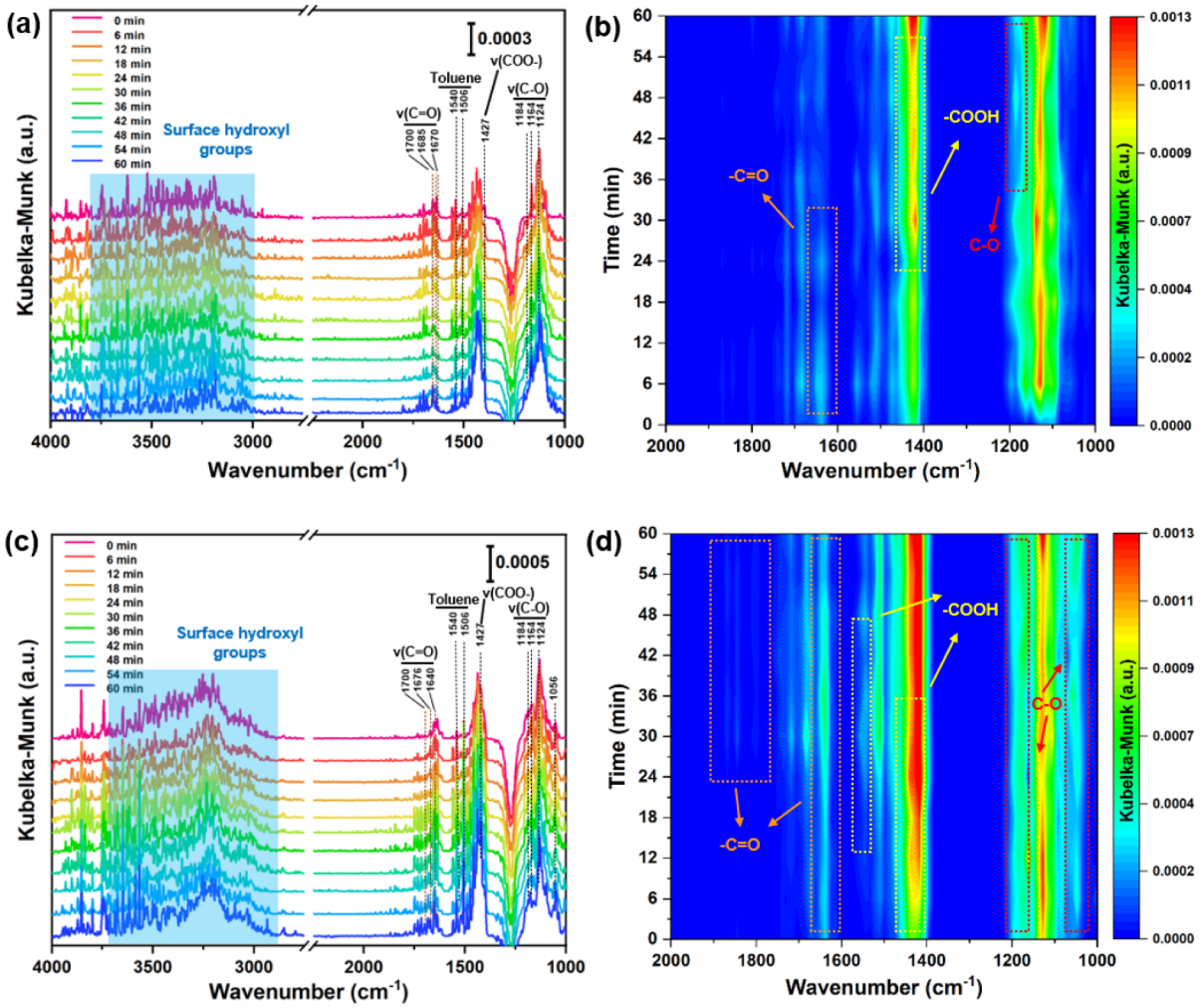

Figure 5. *In situ* DRIFTS of toluene oxidation on (a, b) KM and (c, d) Zn-KM under the condition of H_2O in light.

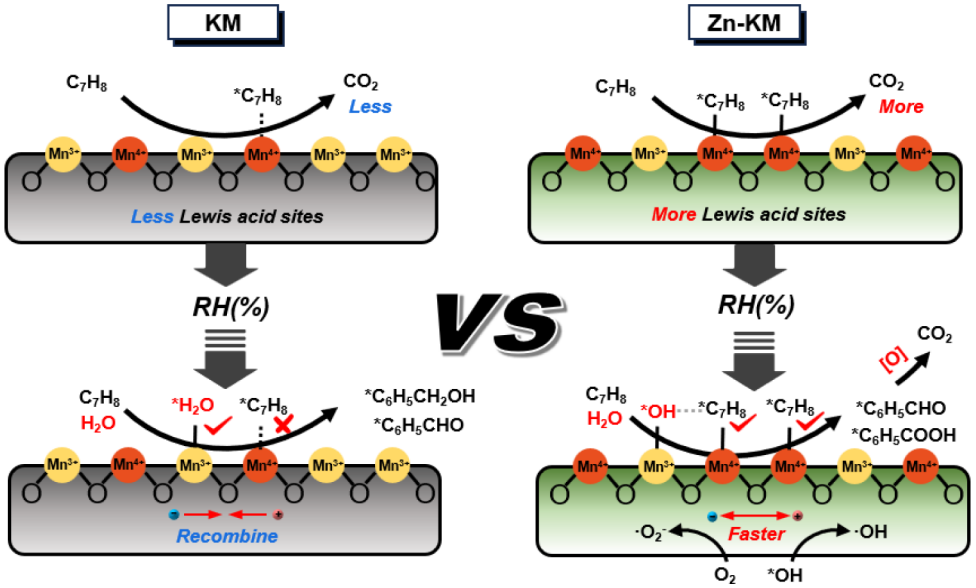

Figure 6. Possible degradation route of toluene over KM and Zn-KM catalysts.

asymmetry and symmetry vibrations of benzoate (1427 and 1550 cm^{-1}), aldehyde species (1670, 1685, 1700, and 1845 cm^{-1}), and O−H stretching vibrations of the surface hydroxyl groups (3000−4000 cm^{-1}). First, the bands at 1124, 1164, and 1184 cm^{-1} appeared; it could be attributed to the benzyl alcohol conversed from the adsorbed toluene, which appeared

https://doi.org/10.1021/acs.jpcc.4c05307
J. Phys. Chem. C 2024, 128, 16522−16531

earlier in Zn-KM, suggesting that the conversion of toluene into benzyl alcohol was easier than KM. In addition, more dominant intermediates of benzaldehyde (1670, 1685, and 1700 cm^{-1}) and benzoic acid (1550 and 1427 cm^{-1}) were observed in Zn-KM, than in KM, suggesting that the routes of benzyl alcohol to benzaldehyde and benzoic acid were faster with the help of better redox ability of Zn-KM. Moreover, as shown in Figure 5b, it is worth noting that the band at 1056 cm^{-1} attributed to alkoxide species appeared only in Zn-KM,[41] further illustrating that Zn-KM owned better ability of opening the ring of toluene. Therefore, owing to better toluene adsorption, faster charge transfer in H_2O enhanced built-in electric field, and the larger amount of ROS species, Zn-KM performed better catalytic activity of toluene oxidation under the condition of H_2O. While as shown in Figure 5d, the band at 1845 cm^{-1} of stretching vibration of aldehyde groups was only observed from Zn-KM. As the better electron pair separation profited from the inner electric field created by H_2O adsorption, the larger amount of ROS species, and better utilization of light, Zn-KM performed better catalytic activity of toluene oxidation under the condition of H_2O.

In all, the toluene oxidation route in the presence of H_2O on Zn-KM and KM are shown in Figure 6, respectively. On Zn-KM: (1) First, the introduction of H_2O promoted the adsorption of toluene under the hydrogen bonding interaction and the surface −OH groups were generated. (2) Under illumination, the photogenerated charge transferred faster in the H_2O-enhanced built-in electric field, and richer active oxygen species ($\cdot O_2^-$ and ·OH radicals) accelerated the oxidation reaction, and then, the adsorbed toluene was oxidated into benzyl alcohol, benzaldehyde, and benzoic acid. (3) Furthermore, the ring-opened generated key intermediate of alkoxide species was generated, which finally mineralized carbon dioxide and water. While, on KM, owing to its surface hydrophilicity, H_2O preferentially adsorbed on its surface, preventing the adsorption and oxidation of toluene, leading to less key ring-opened intermediate and poorer photocatalytic performance.

4. CONCLUSIONS

In this work, the synthesized Zn^{2+}-doped K-OMS-2 (Zn-KM photocatalyst) exhibited improved photocatalytic performance of toluene oxidation in the RH from 10% to 50%, and Zn-KM had better conversion and stability than KM. The doped Zn^{2+} generated more Mn^{4+} in Zn-KM, which acted as Lewis acid sites for toluene adsorption. Importantly, on Zn-KM, the reaction conditions with H_2O promoted toluene adsorption under hydrogen bonding and the intensive built-in electric field, leading to faster charge transfer for more active oxygen-containing radicals, and thus, toluene degradation was enhanced. Whereas, too strong H_2O adsorption on KM inhibited toluene oxidation.

■ ASSOCIATED CONTENT

Supporting Information

The Supporting Information is available free of charge at https://pubs.acs.org/doi/10.1021/acs.jpcc.4c05307.

Structural and morphological characterization of Zn-KM and KM were determined by scanning electron microscopy and XRD. The chemical properties of the Zn-KM and KM surfaces were determined by XPS, H_2-TPR, water contact angle, EIS Nyquist plots, UV−vis DRS, and Py IR (PDF)

■ AUTHOR INFORMATION

Corresponding Authors

Weixin Zou − *State Key Laboratory of Pollution Control and Resource Reuse, School of Environment, Jiangsu Key Laboratory of Vehicle Emissions Control, Center of Modern Analysis, Nanjing University, Nanjing 210023, PR China;* orcid.org/0000-0001-5001-2841; Email: wxzou2016@nju.edu.cn

Qing Tong − *State Key Laboratory of Pollution Control and Resource Reuse, School of Environment, Jiangsu Key Laboratory of Vehicle Emissions Control, Center of Modern Analysis, Nanjing University, Nanjing 210023, PR China;* Email: tongqing@nju.edu.cn

Authors

Xiaoshan Zeng − *State Key Laboratory of Pollution Control and Resource Reuse, School of Environment, Jiangsu Key Laboratory of Vehicle Emissions Control, Center of Modern Analysis, Nanjing University, Nanjing 210023, PR China*

Zehui Huang − *State Key Laboratory of Pollution Control and Resource Reuse, School of Environment, Jiangsu Key Laboratory of Vehicle Emissions Control, Center of Modern Analysis, Nanjing University, Nanjing 210023, PR China*

Xiaoqian Wei − *State Key Laboratory of Pollution Control and Resource Reuse, School of Environment, Jiangsu Key Laboratory of Vehicle Emissions Control, Center of Modern Analysis, Nanjing University, Nanjing 210023, PR China*

Pingping Yu − *State Key Laboratory of Pollution Control and Resource Reuse, School of Environment, Jiangsu Key Laboratory of Vehicle Emissions Control, Center of Modern Analysis, Nanjing University, Nanjing 210023, PR China*

Bin Gao − *Department of Civil and Environmental Engineering, Rensselaer Polytechnic Institute, Troy, New York 12180, United States*

Lin Dong − *State Key Laboratory of Pollution Control and Resource Reuse, School of Environment, Jiangsu Key Laboratory of Vehicle Emissions Control, Center of Modern Analysis, Nanjing University, Nanjing 210023, PR China;* orcid.org/0000-0002-8393-6669

Complete contact information is available at: https://pubs.acs.org/10.1021/acs.jpcc.4c05307

Notes

The authors declare no competing financial interest.

■ ACKNOWLEDGMENTS

This work was supported by the National Natural Science Foundation of China (62375120, 22476085, and 22106067) and Natural Science Foundation of Jiangsu Province of China (BK20240171 and BK20231513).

■ REFERENCES

(1) Lewis, A. C.; Jenkins, D.; Whitty, C. J. M. Hidden harms of indoor air pollution - five steps to expose them. *Nature* **2023**, *614*, 220−223.

(2) Sethi, S.; Nanda, R.; Chakraborty, T. Clinical application of volatile organic compound analysis for detecting infectious diseases. *Clin. Microbiol. Rev.* **2013**, *26*, 462−475.

(3) Dumdei, B.; O'Brien, R. J. Toluene degradation products in simulated atmospheric conditions. *Nature* **1984**, *311*, 248−250.

(4) Dimotakis, E. D.; Cal, M. P.; Economy, J.; Rood, M. J.; Larson, S. M. Chemically treated activated carbon cloths for removal of volatile organic carbons from gas streams: Evidence for enhanced physical adsorption. *Environ. Sci. Technol.* **1995**, *29*, 1876−1880.
(5) Shen, Y. J.; Deng, J.; Hu, X. N.; Chen, X.; Yang, H. Q.; Cheng, D. H.; Zhang, D. S. Expediting toluene combustion by harmonizing the Ce-O strength over Co-doped CeZr oxide catalysts. *Environ. Sci. Technol.* **2023**, *57*, 1797−1806.
(6) Ardizzone, S.; Bianchi, C. L.; Cappelletti, G.; Naldoni, A.; Pirola, C. Photocatalytic degradation of toluene in the gas phase: Relationship between surface species and catalyst features. *Environ. Sci. Technol.* **2008**, *42*, 6671−6676.
(7) Zhang, J. W.; Shen, B. X.; Hu, Z. Z.; Zhen, M. M.; Guo, S. Q.; Dong, F. Uncovering the synergy between Mn substitution and O vacancy in ZnAl-LDH photocatalyst for efficient toluene removal. *Appl. Catal., B* **2021**, *296*, 120376.
(8) Debono, O.; Thevenet, F.; Gravejat, P.; Hequet, V.; Raillard, C.; Lecoq, L.; Locoge, N. Toluene photocatalytic oxidation at ppbv levels: Kinetic investigation and carbon balance determination. *Appl. Catal., B* **2011**, *106*, 600−608.
(9) Xu, J.; Zhang, Q.; Gao, X.; Wang, P.; Che, H.; Tang, C.; Ao, Y. Highly efficient Fe^{III}-initiated self-cycled Fenton system in piezo-catalytic process for organic pollutants degradation. *Angew. Chem., Int. Ed.* **2023**, *62*, No. e202307018.
(10) Zhang, Q.; Chen, J.; Gao, X.; Che, H. N.; Wang, P. F.; Ao, Y. H. In-depth insight into the mechanism on photocatalytic synergistic removal of antibiotics and Cr (VI): The decisive effect of antibiotic molecular structure. *Appl. Catal., B* **2022**, *313*, 121443.
(11) Wu, Y.; Che, H.; Liu, B.; Ao, Y. Promising materials for photocatalysis-self-Fenton system: properties, modifications, and applications. *Small Struct.* **2023**, *4*, 2200371.
(12) Wu, Y.; Wang, P.; Che, H.; Liu, W.; Tang, C.; Ao, Y. Triggering dual two-electron pathway for H_2O_2 generation by multiple $[Bi\text{-}O]_n$ interlayers in ultrathin $Bi_{12}O_{17}Cl_2$ towards efficient piezo-self-Fenton. *Angew. Chem., Int. Ed.* **2024**, *136*, No. e202316410.
(13) Yang, W. H.; Peng, Y.; Wang, Y.; Wang, Y.; Liu, H.; Su, Z.; Yang, W. N.; Chen, J. J.; Si, W. Z.; Li, J. H. Controllable redox-induced in-situ growth of MnO_2 over Mn_2O_3 for toluene oxidation: Active heterostructure interfaces. *Appl. Catal., B* **2020**, *278*, 119279.
(14) Zeng, X. S.; Shan, C. J.; Sun, M. D.; Ding, D. N.; Rong, S. P. Graphene enhanced α-MnO_2 for photothermal catalytic decomposition of carcinogen formaldehyde. *Chin. Chem. Lett.* **2022**, *33*, 4771−4775.
(15) Li, J. H.; Wang, R. H.; Hao, J. M. Role of lattice oxygen and Lewis acid on ethanol oxidation over OMS-2 catalyst. *J. Phys. Chem. C* **2010**, *114*, 10544−10550.
(16) Deng, H.; Kang, S. Y.; Ma, J. Z.; Zhang, C. B.; He, H. Silver incorporated into cryptomelane-type manganese oxide boosts the catalytic oxidation of benzene. *Appl. Catal., B* **2018**, *239*, 214−222.
(17) Zhang, M.; Li, G. H.; Li, Q.; Chen, J.; Elimian, E. A.; Jia, H. P.; He, H. In situ construction of manganese oxide photothermocatalysts for the deep removal of toluene by highly utilizing sunlight energy. *Environ. Sci. Technol.* **2023**, *57*, 4286−4297.
(18) Rong, S.; Zhang, P. Y.; Liu, F.; Yang, Y. J. Engineering crystal facet of α-MnO_2 nanowire for highly efficient catalytic oxidation of carcinogenic airborne formaldehyde. *ACS Catal.* **2018**, *8*, 3435−3446.
(19) Hao, Y.; Sun, S.; Du, X.; Qu, J.; Li, L.; Yu, X.; Zhang, X. H.; Yang, X.; Zheng, R.; Cairney, M. J.; et al. Boosting oxygen reduction activity of manganese oxide through strain effect caused by ion insertion. *Small* **2022**, *18*, 2105201.
(20) Alfaruqi, M. H.; Mathew, V.; Gim, J.; Kim, S. J.; Song, J. J.; Baboo, J.; Choi, S.; Kim, J. Electrochemically induced structural transformation in a γ-MnO_2 cathode of a high capacity zinc-ion battery system. *Chem. Mater.* **2015**, *27*, 3609−3620.
(21) Alfaruqi, M. H.; Gim, J.; Kim, S.; Song, J. J.; Jo, J.; Kim, S.; Mathew, V.; Kim, J. Enhanced reversible divalent zinc storage in a structurally stable α-MnO_2 nanorod electrode. *J. Power Sources* **2015**, *288*, 320−327.
(22) Zhang, N. Q.; Li, L. C.; Guo, Y. Z.; He, J. D.; Wu, R.; Song, L. Y.; Zhang, G. Z.; Zhao, J. S.; Wang, D. S.; He, H. A MnO_2-based catalyst with H_2O resistance for NH_3-SCR: Study of catalytic activity and reactants-H_2O competitive adsorption. *Appl. Catal., B* **2020**, *270*, 118860.
(23) Zhang, X. D.; Bi, F. K.; Zhu, Z. Q.; Yang, Y.; Zhao, S. H.; Chen, J. F.; Lv, X. T.; Wang, Y. X.; Xu, J. C.; Liu, N. The promoting effect of H_2O on rod-like $MnCeO_x$ derived from MOFs for toluene oxidation: A combined experimental and theoretical investigation. *Appl. Catal., B* **2021**, *297*, 120393.
(24) Wei, X. Q.; Li, K.; Zhang, X. Y.; Tong, Q.; Ji, J. W.; Cai, Y. D.; Gao, B.; Zou, W. X.; Dong, L. CeO_2 nanosheets with anion-induced oxygen vacancies for promoting photocatalytic toluene mineralization: Toluene adsorption and reactive oxygen species. *Appl. Catal., B* **2022**, *317*, 121694.
(25) Kresse, G.; Furthmüller, J. Efficiency of Ab-Initio total energy calculations for metals and semiconductors using a plane-wave basis set. *Comput. Mater. Sci.* **1996**, *6*, 15−50.
(26) Kresse, G.; Furthmüller, J. Efficient iterative schemes for Ab initio total-energy calculations using a plane-wave basis set. *Phys. Rev. B* **1996**, *54*, 11169−11186.
(27) Perdew, J. P.; Burke, K.; Ernzerhof, M. Generalized gradient approximation made simple. *Phys. Rev. Lett.* **1996**, *77*, 3865−3868.
(28) Kresse, G.; Joubert, D. From ultrasoft pseudopotentials to the projector augmented-wave method. *Phys. Rev. B* **1999**, *59*, 1758−1775.
(29) Blöchl P, E. Projector augmented-wave method. *Phys. Rev. B* **1994**, *50*, 17953.
(30) Grimme, S.; Antony, J.; Ehrlich, S.; Krieg, H. A consistent and accurate ab initio parametrization of density functional dispersion correction (DFT-D) for the 94 elements H-Pu. *J. Chem. Phys.* **2010**, *132*, 154104.
(31) Bader, R. F. W. A quantum theory of molecular structure and its applications. *Chem. Rev.* **1991**, *91*, 893−928.
(32) Henkelman, G.; Arnaldsson, A.; Jónsson, H. A fast and robust algorithm for Bader decomposition of charge density. *Comput. Mater. Sci.* **2006**, *36*, 354−360.
(33) Hao, Z. F.; Shen, Z. R.; Li, Y.; Wang, H. T.; Zheng, L. R.; Wang, R. H.; Liu, G. Q.; Zhan, S. H. The role of alkali metal in α-MnO_2 catalyzed ammonia-selective catalysis. *Angew. Chem., Int. Ed.* **2019**, *58*, 6351−6356.
(34) Li, Y. Z.; Fan, Z. Y.; Shi, J. W.; Liu, Z. Y.; Zhou, J. W.; Shangguan, W. F. Modified manganese oxide octahedral molecular sieves M'-OMS-2 (M'=Co, Ce, Cu) as catalysts in post plasma-catalysis for acetaldehyde degradation. *Catal. Today* **2015**, *256*, 178−185.
(35) Zhong, L.; Brancho, J. J.; Batterman, S.; Barlett, B. M.; Godwin, C. Experimental and modeling study of visible light responsive photocatalytic oxidation (PCO) materials for toluene degradation. *Appl. Catal., B* **2017**, *216*, 122−132.
(36) Liu, B.; Zhan, Y.; Xie, R.; Huang, H.; Li, K.; Zeng, Y.; Shrestha, R. P.; Oanh, N. T. K.; Winijkul, E. Efficient photocatalytic oxidation of gaseous toluene in a bubbling reactor of water. *Chemosphere* **2019**, *223*, 754−761.
(37) Mo, J.; Zhang, Y.; Xu, Q. Effect of water vapor on the by-products and decomposition rate of ppb-level toluene by photocatalytic oxidation. *Appl. Catal., B* **2013**, *132*, 212−218.
(38) You, J. W.; Vikrant, K.; Lim, D. H.; Verma, S.; Kukkar, D.; Anwer, H.; Kim, K. H. Photocatalytic potential of a titanium dioxide−supported platinum catalyst against VOCs with complicated composition under varying humidity conditions. *J. Cleaner Prod.* **2022**, *371*, 133487.
(39) Zhao, W. R.; Dai, J. S.; Liu, F. F.; Bao, J. Z.; Wang, Y.; Yang, Y.; Yang, Y. N.; Zhao, D. Y. Photocatalytic oxidation of indoor toluene: Process risk analysis and influence of relative humidity, photocatalysts, and VUV irradiation. *Sci. Total Environ.* **2012**, *438*, 201−209.
(40) Mi, R.; Li, D.; Hu, Z.; Yang, R. T. Morphology effects of CeO_2 nanomaterials on the catalytic combustion of toluene: a combined

https://doi.org/10.1021/acs.jpcc.4c05307
J. Phys. Chem. C 2024, 128, 16522−16531

kinetics and diffuse reflectance infrared fourier transform spectroscopy study. *ACS Catal.* **2021**, *11*, 7876−7889.
(41) Zhang, L. X.; Zhu, Z. X.; Tan, W.; Ji, J. W.; Cai, Y. D.; Tong, Q.; Xiong, Y.; Wan, H. Q.; Dong, L. Thermal-driven optimization of the strong metal−support interaction of a platinum-manganese oxide octahedral molecular sieve to promote toluene oxidation: effect of the interface Pt^{2+}-O_v-$Mn^{\delta+}$. *ACS Appl. Mater. Interfaces* **2022**, *14*, 56790−56800.
(42) Hao, Y. X.; Hung, S. F.; Zeng, W. J.; Wang, Y.; Zhang, C. C.; Kuo, C.; Wang, L. Q.; Zhao, S.; Zhang, Y.; Chen, H.; et al. Switching the oxygen evolution mechanism on atomically dispersed Ru for enhanced acidic reaction kinetics. *J. Am. Chem. Soc.* **2023**, *145*, 23659−23669.
(43) Ye, L.; Lu, P.; Xianhui, Y.; Huang, H. Boosting simultaneous catalytic removal of NO_x and toluene via cooperation of Lewis acid and oxygen vacancies. *Appl. Catal., B* **2023**, *331*, 122696.
(44) Chen, Z. C.; Ouyang, Q.; Du, W.; Chen, Y. C. Palladium (0) π-Lewis base catalysis: concept and development. *J. Am. Chem. Soc.* **2024**, *146*, 6422−6437.
(45) Gao, F. Y.; Tang, X. L.; Yi, H. H.; Li, J. Y.; Zhao, S. Z.; Wang, J. E.; Chu, C.; Li, C. L. Promotional mechanisms of activity and SO_2 tolerance of Co- or Ni-doped MnO_x-CeO_2 catalysts for SCR of NO_x with NH_3 at low temperature. *Chem. Eng. J.* **2017**, *317*, 20−31.
(46) Lin, F.; Wang, Z. H.; Ma, Q.; Yang, Y.; Whiddon, R.; Zhu, Y. Q.; Cen, K. F. Catalytic deep oxidation of NO by ozone over MnO_x loaded spherical alumina catalyst. *Appl. Catal., B* **2016**, *198*, 100−111.
(47) Wang, M.; Zhang, Y.; Yu, Y. B.; Shan, W. P.; He, H. Synergistic effects of multicomponents produce outstanding soot oxidation activity in a Cs/Co/MnO_x catalyst. *Environ. Sci. Technol.* **2021**, *55*, 240−248.
(48) Zhang, B. G.; Shen, Y. J.; Liu, B. Y.; Ji, J.; Dai, W. J.; Huang, P. L.; Zhang, D. S.; Li, G. Q.; Xie, R. J.; Huang, H. B. Boosting Ozone catalytic oxidation of toluene at room temperature by using hydroxyl-mediated MnO_x/Al_2O_3 catalysts. *Environ. Sci. Technol.* **2023**, *57*, 7041−7050.
(49) Yu, P.; Li, N.; Zou, W.; Wei, X.; Ji, J. W.; Han, L.; Cai, Y.; Tan, W.; Gao, B.; Dong, L. K^+ and CeO_2 nanoparticles modified OMS-2 nanorods for enhanced activity and stability of photocatalytic toluene oxidation: K^+ charge modulation and mechanistic investigation. *Chem. Eng. J.* **2023**, *451*, 138943.
(50) Jiang, S. L.; Li, C. H.; Muhammad, Y.; Tang, Y.; Wang, R. M.; Li, J. J.; Li, J.; Zhao, Z. X.; Zhao, Z. X. Solvent-induced fabrication of Cu/MnO_x nanosheets with abundant oxygen vacancies for efficient and long-lasting photothermal catalytic degradation of humid toluene vapor. *Appl. Catal., B* **2023**, *328*, 122509.
(51) Chen, T.; Dou, H. Y.; Li, X. L.; Tang, X. F.; Li, J. H.; Hao, J. M. Tunnel structure effect of manganese oxides in complete oxidation of formaldehyde. *Microporous Mesoporous Mater.* **2009**, *122*, 270−274.
(52) Mo, S. P.; Zhang, Q.; Li, J. Q.; Sun, Y. H.; Ren, Q. M.; Zou, S. B.; Zhang, Q.; Lu, J. H.; Fu, M. L.; Mo, D. Q.; et al. Highly efficient mesoporous MnO_2 catalysts for the total toluene oxidation: Oxygen-Vacancy defect engineering and involved intermediates using *in situ* DRIFTS. *Appl. Catal., B* **2020**, *264*, 118464.
(53) Wu, Y. S.; Lu, Y.; Song, C. J.; Ma, Z. H.; Xing, S. T.; Gao, Y. Z. A novel redox-precipitation method for the preparation of α-MnO_2 with a high surface Mn^{4+} concentration and its activity toward complete catalytic oxidation of o-xylene. *Catal. Today* **2013**, *201*, 32−39.
(54) Wan, X.; Shi, K.; Li, H.; Shen, F. X.; Gao, S.; Duan, X. M.; Zhang, S.; Zhao, C. N.; Yu, M.; Hao, R. T.; et al. Catalytic ozonation of polluter benzene from −20 to > 50 °C with high conversion efficiency and selectivity on mullite YMn_2O_5. *Environ. Sci. Technol.* **2023**, *57*, 8435−8445.
(55) Wang, B.; Zhuo, Z.; Li, H.; Liu, S.; Zhao, S.; Zhang, X.; Liu, J.; Xiao, D.; Yang, W.; Yu, H. Stacking faults inducing oxygen anion activities in Li_2MnO_3. *Adv. Mater.* **2023**, *35*, 2207904.
(56) Liu, W.; Bai, P.; Wei, S.; Yang, C.; Xu, L. Gadolinium changes the local electron densities of Nickel 3d orbitals for efficient electrocatalytic CO_2 reduction. *Angew. Chem., Int. Ed* **2022**, *61*, No. e202201166.
(57) Li, H. W.; Ho, W. K.; Cao, J. J.; Park, D.; Lee, S. C.; Huang, Y. Active complexes on engineered crystal facets of MnO_x-CeO_2 and scale-up demonstration on an air cleaner for indoor formaldehyde removal. *Environ. Sci. Technol.* **2019**, *53*, 10906−10916.
(58) Zhang, Z. M.; Lin, F. W.; Xiang, L.; Yu, H. D.; Wang, Z. H.; Yan, B. B.; Chen, G. Y. Synergistic effect for simultaneously catalytic ozonation of chlorobenzene and NO over $MnCoO_x$ catalysts: byproducts formation under practical conditions. *Chem. Eng. J.* **2022**, *427*, 130929−130943.
(59) Jockusch, S.; Turro, N. J.; Tomalia, D. A. Aggregation of methylene blue adsorbed on starburst dendrimers. *Macromolecules* **1995**, *28*, 7416−7418.
(60) Ovchinnikov, O. V.; Evtukhova, A. V.; Kondratenko, T. S.; Smirnov, M. S.; Khokhlov, V. Y.; Erina, O. V. Manifestation of intermolecular interactions in FTIR spectra of methylene blue molecules. *Vib. Spectrosc.* **2016**, *86*, 181−189.
(61) Quintão, A. D.; Coutinho, K.; Canuto, S. Theoretical study of the hydrogen bond interaction between methylene blue and water and possible role on energy transfer for photodynamics. *Int. J. Quantum Chem.* **2002**, *90*, 634−640.
(62) Stoerzinger, K. Z.; Risch, M.; Han, B. H.; Shao-Horn, Y. Recent insights into manganese oxides in catalyzing oxygen reduction kinetics. *ACS Catal.* **2015**, *5*, 6021−6031.
(63) Imai, K.; Fukushima, T.; Kobayashi, H.; Higashimoto, S. Visible-light responsive TiO_2 for the complete photocatalytic decomposition of volatile organic compounds (VOCs) and its efficient acceleration by thermal energy. *Appl. Catal., B* **2024**, *346*, 123745.
(64) Dong, X.; Cui, W.; Wang, H.; Li, J.; Sun, Y.; Wang, H. Q.; Zhang, Y.; Huang, H.; Dong, F. Promoting ring-opening efficiency for suppressing toxic intermediates during photocatalytic toluene degradation via surface oxygen vacancies. *Sci. Bull.* **2019**, *64*, 669−678.
(65) Dong, X.; Cui, Z.; Sun, Y.; Dong, F. Humidity-independent photocatalytic toluene mineralization benefits from the utilization of edge hydroxyls in layered double hydroxides (LDHs): A combined operando and theoretical investigation. *ACS Catal.* **2021**, *11*, 8132−8139.
(66) Li, Y.; Chen, B.; Liu, L.; Zhu, B.; Zhang, D. Q. Water-Resistance-Based S-Scheme heterojunction for deep mineralization of toluene. *Angew. Chem., Int. Ed.* **2024**, *11*, No. e202319432.

https://doi.org/10.1021/acs.jpcc.4c05307
J. Phys. Chem. C 2024, 128, 16522−16531